High-level Multireference Investigations on the Electronic States in Single-Vacancy (SV) Graphene Defects Using a Pyrene-SV Model

Reed Nieman,[1,a] Vytor P. Oliveira,[2,a] Bhumika Jayee,[1,a,b] Adelia. J. A. Aquino,[3] Francisco B. C. Machado,[2]* Hans Lischka[1]*

[1] Department of Chemistry and Biochemistry, Texas Tech University Lubbock, TX 79409-1061, USA

[2] Departamento de Química, Instituto Tecnológico da Aeronáutica, São José dos Campos, 122228-900, SP, Brazil

[3] Department of Mechanical Engineering, Texas Tech University, Lubbock, TX, 79409, USA

[a] These authors contributed equally to this publication.

[b] Current address: Department of Chemistry and Chemical Biology, Northeastern University, Boston MA, 02115, USA

Email Hans Lischka: Hans.Lischka@ttu.edu

Email Francisco B. C. Machado: fmachado@ita.br

Abstract

The nonplanar character of graphene with a single carbon vacancy defect (SV) is investigated utilizing a pyrene-SV model system by way of complete active space self-consistent field theory (CASSCF) and multi-reference configuration interaction singles and doubles (MR-CISD) calculations. Planar structures were optimized with both methods showing the $^3B_1$ state as the ground state with three energetically close states within an energy range of 1 eV. These planar structures constitute saddle-points. However, upon following the out-of-plane imaginary frequency yields more stable (by 0.22 to 0.53 eV), but non-planar structures of C_S symmetry. Of these, the $^1A'$ structure is the lowest in energy and is strongly deformed into an L-shape. Following a further out-of-plane imaginary frequency in the non-planar structures leads to the most stable, but most deformed singlet structure of C_1 symmetry. In this structure a bond is formed between the carbon atom with the dangling bond and a carbon of the cyclopentadienyl ring. This bond stabilizes the structure by more than 3 eV compared to the planar $^3B_1$ structure. Higher excited states were calculated at MR-CISD level showing a grouping of four states low in energy and higher states starting around 3 eV.

1. Introduction

Graphene is a fascinating and promising material which has been discovered in 2004 by Geim and Novoselov.[1] Graphene is a single layer of graphite with exceptional electronic, thermal and mechanical properties, as well as promising applications in electronics, optoelectronics and photonics.[2-8] To create appropriate semiconductor properties for graphene, its semimetal character has to be modified. This goal is frequently achieved by the introduction of defects. Vacancy defects provide a good opportunity to achieve strong variations in the electronic properties of graphene. This class of defects in graphene sheets can arise either during defective growth or after irradiation of the material.[9] Such defects change the material's electronic properties. By the removal of carbon atoms from the regular honeycomb network,[10, 11] dangling bonds are created,[12, 13] which lead to an open shell character of the defects and the induction of magnetism.[14-16] The open shell character of the electronic structure will lead to the occurrence of low-lying electronic states and gives rise to complex geometric variations. In the case of a single carbon vacancy, one carbon atom is missing in the regular hexagon and one dangling bond occurs in the relaxed structure. The structural details of this defect were observed using transmission electron microscopy (TEM)[10, 11, 17, 18] and scanning tunneling microscopy (STM)[19, 20] experiments.

The knowledge about the structure and energetics of defects in the structures of polycyclic aromatic hydrocarbon (PAH's) also plays an important role in aerospace technology. Space vehicles' re-entrance into Earth's atmosphere occurs at hypersonic speeds, exposing the surface of the vehicle to temperatures beyond 2,000 K and to highly reactive species such as O and N formed from dissociated air molecules.[21] A thermal protective system (TPS) minimizes erosion of the surface. The TPS are usually graphitic-based materials utilized due to their light weight, high durability, thermal, and mechanical resistance.[22] Recently, molecular beam-surface scattering experiments[23-26] have shown that hyperthermal O and N interaction with highly oriented pyrolytic graphite (HOPG) may result in multiple processes involving carbon ablation, oxidation, and nitridation, which are affected by temperature and presence of defects. Computational dynamics simulations of hyperthermal N and O collision with graphene sheets with and without vacancy defects[27-30] provided an understanding on the mechanism of atom insertion on vacancies, graphene functionalization and ejection of diverse molecules, such as CO, CN, CO_2, O_2 and N_2. However, the occurrence of dangling bonds in the vacancy defect structures makes the system more unstable with a high polyradical character and closely spaced, low-lying excited states with different spin

multiplicities. Although, static DFT calculations[13] and dynamics simulations based on semiempirical and DFT calculations[27, 28, 31] may describe chemically relevant bond breaking/formation events, multireference methods[32, 33] are certainly to be preferred to reliably describe the complex open shell character of the quasi-degenerate states of different spin symmetry occurring in defected graphene structures. The experience with properly calculating the manifolded electronic structure of graphene vacancy defects is crucial for the development of reliable potential energy functions to be used e.g. in the mentioned respective hyperthermal collision simulations involving graphene sheets.

In previous works, we investigated the effect of inducing a single (SV) and a double vacancy (DV) to pristine pyrene, a reduced graphene model system. The geometry relaxation process,[12, 34] the reactivity toward atomic hydrogen,[31, 35] the addition of Si dopant,[36] the extension of the model system to circumpyrene and 7a,7z-periacene[13] were explored. These studies were carried out using both multireference (MR) methods and for larger systems with density functional theory (DFT). These investigations showed that vacancy defects indeed induce the formation of several low-lying excited states of triplet and singlet multiplicity and that ΔSCF-DFT calculations applicable to selected symmetry cases could reproduce the results obtained with MR methods well even though nonnegligible differences between different functionals were observed. More critical is the fact that time-dependent DFT (TD-DFT) was found to be sensitive to the MR character of the chosen reference state. Similar experience has been reported in systematic comparison of different MR methods with DFT for hexagonal boron nitride defect sites by Reimers et al.[37]

The objective of the present study is to provide a systematic investigation of the combination of geometry and electronic changes that takes place by allowing pyrene-1C to distort from planar C_{2V} conformation into non-planar C_s and C_1 conformations. This study is the first step into a complete consideration of how extension of the π-system may hinder/minimize out-of-planar deformation in graphene sheets. Both for the planar and non-planar conformations, the characterization of several low-lying singlet and triplet electronic states which arise from the SV defect will be discussed.

2. Computational Methods

Our previous study[12] has shown that removing a center carbon from pristine pyrene and optimizing the geometry results in the pyrene-1C structure shown in Figure 1. This results in three

dangling bonds, two of which interact to form the C_4-C_5 covalent bond leading to a five member-ring, leaving only one remaining carbon atom with a dangling bond (C_{10}). Four states ($^3B_1$, $^3A_2$, $^1B_1$, and $^1A_2$) close in energy separated by less than 0.1 eV were observed. The energy of pyrene-1C was further decreased by lifting the carbon dangling bond out of the molecular plane lowering the symmetry of the system to C_S.

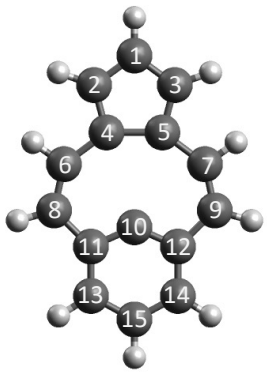

Figure 1. Single vacant pyrene at C_{2V} symmetry.

To better understand the changes in electronic structure responsible for the energy lowering that occurs by breaking the planar geometry, the pyrene-1C geometry was fully optimized using complete active space self-consistent field (CASSCF)[38, 39] and uncontracted multireference configuration interaction calculations with singles and doubles (MR-CISD).[32, 33, 40] Various complete active spaces were tested ranging from a compact four electrons in three orbitals space (4,3) to a CAS(6,6), and finally a large space comprising the complete π-space and the dangling bond orbital at C_{10} (16,16). The shape and functionality of these orbitals are discussed in the Results section. Harmonic frequencies were computed using a compact space, CAS(4,3), to characterize the stationary state geometries as a transition state or a minimum energy point on the potential energy hyper-surface (PES). In view of these extended computational requirements of the geometry characterizations, the standard 6-31G* basis set[41, 42] was chosen for all calculations. It is noted that in previous investigations on different types of multiplet splittings of radical and biradical PAHs,[43] differences between the larger triple-zeta 6-311G(2d) basis and 6-31G* results amounted to only a few hundredths of an eV which is quite a satisfactory agreement in view of the significantly increased computer time required for the former basis set.

Full geometry optimization was carried out for each of the four lowest states of planar pyrene-1C of C_{2V} symmetry ($^3B_1$, $^1B_1$, $^3A_2$, and $^1A_2$), for the four lowest states of the non-planar geometries of C_S symmetry ($^1A'$, $^3A'$, $^1A''$ and $^3A''$) and for the two lowest states of the non-planar geometries of C_1 symmetries (^1A and ^3A). Single state CASSCF and state averaging (SA) over two states and four states (of same symmetry but different multiplicity) were considered. The pyrene-1C molecule at C_{2V} geometry was arranged in the yz-plane with the long axis oriented along the z-axis. The Cartesian coordinates of all optimized geometries are collected in the SI.

The geometries were further optimized using MR-CISD with a CAS(4,3) reference space for the planar C_{2V} and non-planar C_S and C_1 conformations. The characterization of several low-lying singlet and triplet states was carried out using extended MR-CISD calculations with a CAS(6,6) reference space for the planar C_{2v} and non-planar C_s conformations using the SA4-CASSCF(4,3) geometries. Size-extensivity contributions are included by the Davidson correction which is denoted by the label +Q.[33, 44] CASSCF energy and geometry optimization calculations as well as MR-CISD single-point calculations were performed with the COLUMBUS software,[40, 45] whereas CASSCF geometry optimization followed by frequency calculations were performed using Molpro.[46]

3. Discussion and Results

3.1. Choice of the Active Space

Our previous investigations showed that radical character and reactivity of pyrene-1C toward atomic H is concentrated on the carbon with the dangling bond and on the cyclopentadiene ring.[12, 35] Several active spaces were investigated. In the C_{2v} framework, a CAS(6,6) was selected with active orbitals composed of the $25a_1$ orbital, which is the dangling bond on C_{10}, the $3\text{-}4a_2$ and $4\text{-}5b_1$ π-orbitals (Figure 2). An inspection in the natural orbital (NO) occupation numbers of the CASSCF(6,6) calculations of the optimized geometries of the four states ($^3B_1$, $^3A_2$, $^1A_2$ and $^1B_1$) showed the orbital $4b_1$ to remain doubly occupied (occupation number > 1.9) and the orbitals $6b_1$ and $4a_2$ remained empty (occupation numbers ≤ 0.1) for all four states (Table S1 of the Supporting Information (SI)). Removing these orbitals from the active space resulted in a compact CAS(4,3). The CASSCF(4,3) results followed the same relative energy ordering of the states of the CASSCF(6,6) calculations (Table S2). To further verify the suitability of the CASSCF(4,3) and CASSCF(6,6) approaches, we optimized pyrene-1C with a larger CAS(16,16) consisting of the

entire π-space (orbitals of 1-9b_1 and 1-6a_2) plus the carbon dangling bond orbital (25a_1) (Table S2). This larger active space was applied only for calculations that kept the structure at the high C_{2v} symmetry. No significant difference in geometries or relative energies were found when comparing CASSCF(16,16) results to CASSCF(6,6) and SA2-CASSCF(4,3) (Table 1 and Tables S2-S4).

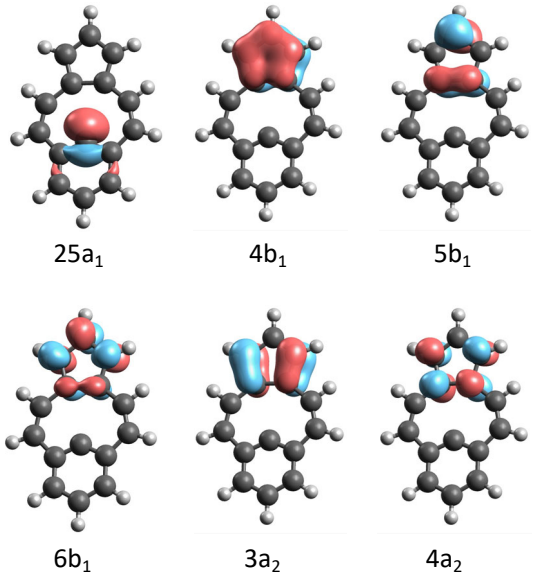

Figure 2. Active molecular orbitals for the $^3B_1$ state computed at the CASSCF(6,6)/6-31G* level.

Table 1. Energy differences (eV) relative to the $^3B_1$ state and optimized C_4-C_5 bond lengths (Å) using the SA4-CASSCF(4,3) and MR-CISD(4,3). Davidson correction indicated with +Q.

Sym.	State	SA4-CASSCF(4,3)		MR-CISD(4,3)		
		ΔE	C4-C5	ΔE	ΔE+Q	C4-C5
C_{2V}	1^3B_1	0.000	1.568	0.000	0.000	1.564
	1^1B_1	0.001	1.565	0.117	0.090	1.564
	1^3A_2	0.107	1.414	0.147	0.133	1.416
	1^1A_2	0.107	1.413	0.189	0.164	1.416
C_S	$1^1A'$	-0.430	1.519	-1.157	-1.129	1.519
	$1^3A'$	-0.015	1.565	0.024	-0.020	1.561
	$1^3A''$	0.047	1.400	0.078	0.043	1.402
	$1^1A''$	0.047	1.399	0.089	0.053	1.402
C_1	1^1A	-2.897	1.522	-3.529	-3.770	1.510
	1^3A	-2.286	1.516	-2.021	-2.221	1.508

3.2. Characterization of the Different Optimized Structures

Harmonic frequency calculations were performed on the optimized geometries at SA2-CASSCF(4,3)/6-31G* level to evaluate the nature of the stationary states found. These calculations were restricted to the averaging of two states of the same multiplicity. Differences in the C_4-C_5 distances between all CASSCF calculations used are small (Table 1, dominant electron configurations are collected in Tables S5). Figure 3 presents a schematic representation of the search for minimum energy geometries guided by an analysis of vibrational modes. Figure S1 shows a detailed description of the geometries and plots of their active orbitals for reference.

Based on the vibrational analysis, pyrene-1C C_{2v} optimized geometries are found to be transition states (TS). An out-of-plane (oop) bending mode with an imaginary frequency is found for the $^3B_1$ state. Following the gradient of this mode leads to a $^3A'$ state of C_s symmetry which is a local minimum just 0.01 eV lower in energy than that of the $^3B_1$ state. The $^3A_2$ state possesses three imaginary modes, one in-plane (ip of b_2 symmetry) and two oop (both of b_1 symmetry). The geometry optimization carried out by a distortion in the direction of the gradient along the ip imaginary mode (orange box of Figure 3) leads to the geometry of the $^3B_1$ state via an intersection of energy surfaces. Also, a distortion in the direction of any of the oop modes (blue box of Figure 3) results in a $^3A''$ state of C_S symmetry, which is 0.06 eV lower than the $^3A_2$ structure, but it is still a transition state geometry. Following the imaginary mode of the $^3A''$ state leads to the same $^3A'$ minimum structure as had already been found starting from the $^3B_1$ geometry. This minimum is just 0.06 eV lower than the $^3A''$ geometry.

The $^1B_1$ state possesses two oop imaginary modes, a distortion in the direction of these modes followed by geometry optimization leads to a $^1A'$ geometry of C_S geometry, which is 0.60 eV lower than the $^1B_1$ geometry, but is still a first order TS. To reach an energy minimum, the C_S symmetry must be broken. C_4-C_{10} bond formation leads to a geometry of C_1 symmetry, a highly stable geometry 2.63 eV lower than $^1A'$, characterized by a non-planar structure possessing four rings. Starting from this ^1A geometry, a similar minimum is also found for the ^3A state, but 1.49 eV higher in energy.

The $^1A_2$ state geometry has two imaginary modes: one ip mode of b_2 symmetry and one oop mode of b_1 symmetry. Following the ip mode leads to the $^1B_1$ state geometry. Whereas by following the oop mode the $^1A''$ minimum geometry is reached.

The energetic stabilities based on optimized geometries can be summarized as follows: for the planar C_{2v} conformations, the lowest energy is observed for the $^3B_1$ state, closely followed by the $^1B_1$, $^3A_2$ and $^1A_2$ states. The difference in energy between the $^3B_1$ and $^1A_2$ geometries is just 0.12 eV. In the non-planar pyrene-1C case with C_S symmetry, the L-shaped conformation of the $^1A'$ state results in a decrease of 0.53 eV compared to the planar $^3B_1$ pyrene-1C structure due to the stability brought by the 3c-2e non-classical interaction between C_{10}, C_4 and C_5 (orbital 29a', Figure S1). Out-of-plane relaxation has a smaller stabilizing effect for the states $^3A'$, $^3A''$, and $^1A''$ which are 0.5 to 0.6 eV higher in energy than the $^1A'$ state geometry. The geometry optimization of these states minimizes exchange-repulsion interactions, but no bonding interaction as the one present in $^1A'$ is formed. Further geometry relaxation from C_S to C_1 symmetry allows the formation of a classical 2c-2e C-C covalent bond, leading to greater stabilization and a larger difference between the energy of singlet and triplet. The ^1A optimized geometry is 3.16 eV lower than the planar $^3B_1$ geometry and 2.14 eV lower than the ^3A geometry. In relation to the geometries, comparing SA2-CASSCF(4,3)/6-31G* (Table S5) to SA2-CASSCF(6,6)/6-31G* (Table S6), there are only small differences and the overall agreement is good. This is especially true for the excitation energies and optimized geometries of the C_{2V} point group. When considering the C_S structures, the geometries are consistent within errors of about 0.012 Å in the maximum for the $^3A'$ structure.

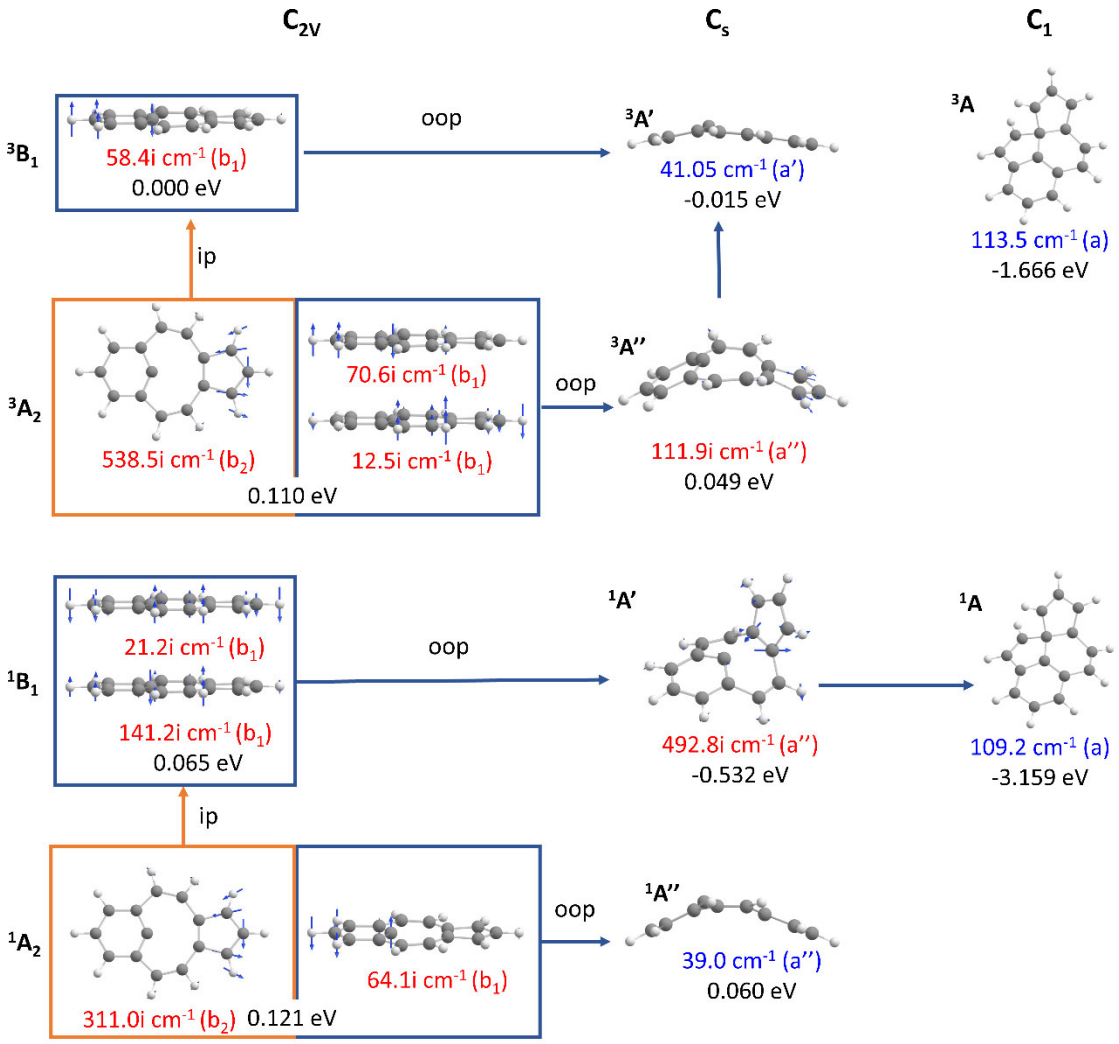

Figure 3. Structures obtained after geometry optimization and followed by harmonic frequencies calculations at SA2-CASSCF(4,3)/6-31G* level of theory. Geometries were distorted and reoptimized according to the force vectors of imaginary frequencies. In-plane (ip) and out-of-plane (oop) force vectors for C_{2V} structures are displayed in orange and blue boxes, respectively. Imaginary frequencies are given in red, the lowest frequency for minima is in blue. The symmetry of normal modes is given in parentheses. Energies given in eV are relative to 1 $^3B_1$.

To better account for dynamic electron correlation effects, all geometries shown in Figure 3 were reoptimized utilizing the MR-CISD(4,3)/6-31G* method. The energies of the MR-CISD(4,3) optimized geometries (Table 1) support the results of the SA4-CASSCF(4,3). The excitation energies of the planar excited states are increased compared to the SA4-CASSCF(4,3) energies, a feature found for the non-planar ^{1}A', ^{3}A', ^{1}A", and ^{3}A structures as well. Conversely, the ^{1}A' and ^{1}A structures are stabilized compared to the planar structure by 0.73 and 0.63 eV,

respectively. The Davidson-corrected values (+Q), change only slightly in most cases, but is as much as 0.25 and 0.20 eV for the ^{1}A and ^{3}A structures, respectively. Figure 4 shows an overview of the obtained structures and provides optimized distances, angles, planes, and plane centroids to characterize the geometry of different states at C_{2v}, C_s, and C_1 symmetries. Overall, the geometries are similar to those obtained for SA4-CASSCF(4,3). Root means square deviations (RMSD) of MR-CISD geometries are below 0.01 Å for states of C_{2V} symmetry and reach a maximum of 0.079 Å for the state ^{3}A of C_1 symmetry. Although CAS(4,3) is a relatively small active space, the good agreement with MR-CISD supports its use.

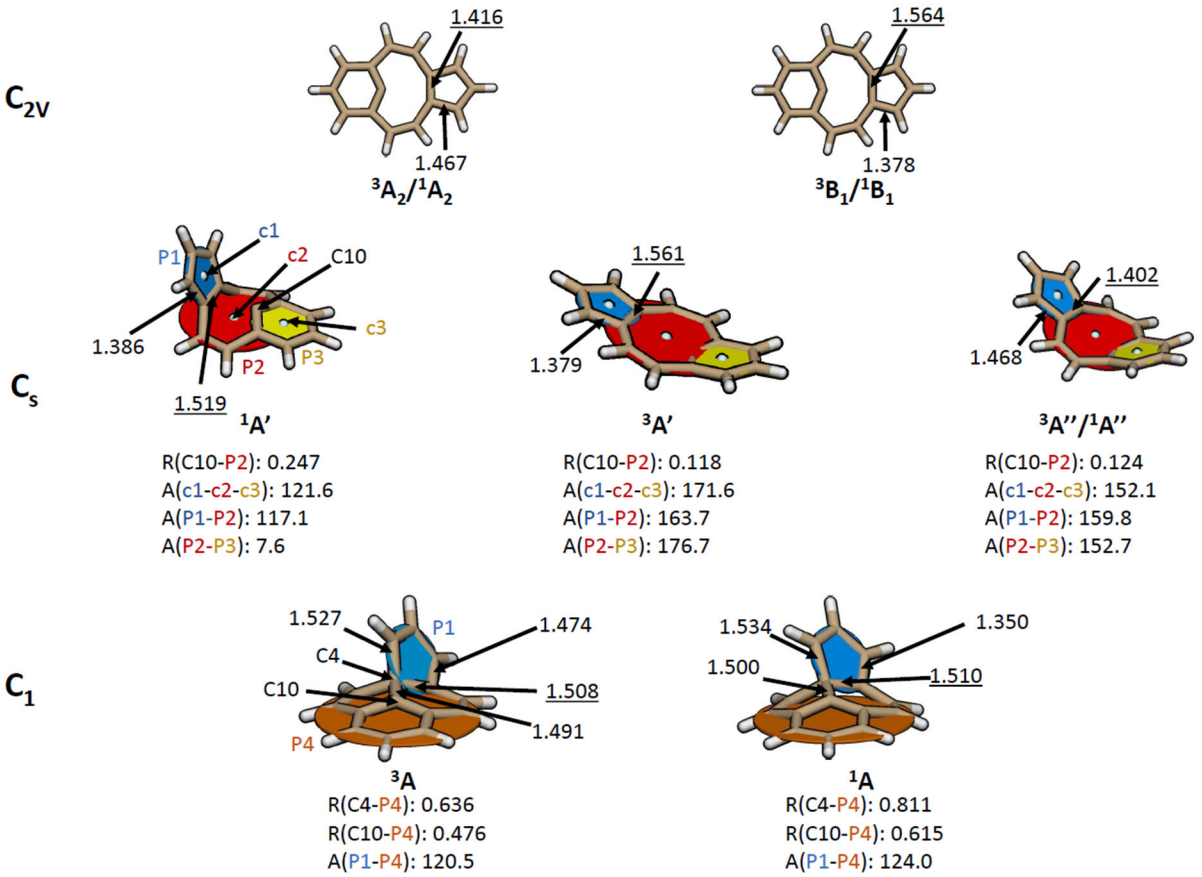

Figure 4. Selected geometric parameter of pyrene-1C obtained for states of C_{2V}, C_S and C_1 symmetry. P1 is the plane fitted to the polygon formed by atoms C_1 to C_5, P2 to the polygon C_6 to C_9, P3 to the polygon C_{11} to C_{14} and P4 to the polygon C_6 to C_9 and C_{13} to C_{15}; c1, c2, c3 are the centroids of the polygons, respectively. The C_4-C_5 bond distances are underlined. Distances are given in Å and angles in degree. Geometries calculated at the MR-CISD(4,3)/6-31G* level of theory.

In C_{2v} symmetry singlet and triplet states have similar geometry, but states of different symmetry (B_1 and A_2) are easily distinguished based on C_4-C_5 and C_2-C_4 bond distances (Figure 4). Geometries optimized for the $^1A_2$ and $^3A_2$ states of C_{2v} symmetry have a somewhat shorter C_4-C_5 distance (1.416 Å for $^3A_2$) than C_2-C_4 (1.467 Å for $^3A_2$), whereas geometries of B_1 symmetry possess a longer C_4-C_5 distance (1.564 Å) compared to C_2-C_4 (1.378 Å). The non-planar geometries obtained from oop distortions in C_s symmetry have different degrees of oop distortion depending on the multiplicity and symmetry (A' or A") of the state. The geometry of the optimized ^{1}A' state in C_s symmetry is almost L-shaped with the plane P3 slightly bent inward, forming a 7.6° angle with the plane P2 and an angle of 117.1° with P1 (Figure 4). The strong deviation from planarity is well described by the angle between the centroids c1-c2-c3 of P1, P2 and P3 which is 121.6°, far from linearity.

On the other side, the optimized ^{3}A' geometry has a shallow bowl shape, featuring a small oop distortion. The angle formed by the centroids of the rings (c1-c2-c3) is almost linear (171.6°) and the dangling bond carbon is just 0.118 Å above the plane of the six-membered ring (P3). Both ^{3}A' and ^{1}A' states have C_4-C_5 and C_2-C_4 bond distances similar to those of the B_1 states of C_{2v} symmetry from which they are derived. Optimized geometries of singlet and triplet states of A" symmetry have similar geometries. Different from ^{3}A', the ^{1}A" and ^{3}A" have a deep bowl shape. The angle formed by the three centroids deviates from linearity by 28°. The C_4-C_5 and C_2-C_4 bond distances of ^{3}A" and ^{1}A" are reminiscent of those of the A_2 state of C_{2V} symmetry. Further distortion of ^{1}A' geometry into the ^{1}A state of C_1 symmetry allows the formation of a covalent bond between C_4 and C_{10} resulting in a geometry that contains four rings. Carbons C_6 to C_9 and C_{13} to C_{15} can be fitted relatively well into a single plane (P4), whereas C_4 and C_{10} are above this plane by 0.811 Å and 0.615 Å, respectively. The plane containing the carbons of the five membered ring (P1) has an angle of 124.0° to P4. The C_4-C_5 bond length is similar to the one in ^{1}A' state of C_S symmetry and $^1B_1$ state of C_{2V} symmetry. Calculation of a triplet state taking ^{1}A as a starting point resulted in a similar geometry, where C_4 and C_{10} are slightly closer to the P4 plane with a similar C_4-C_5 bond distances, indicating that this geometry may not be directly related to the ^{3}A" geometry of C_S symmetry, characterized by a shorter C_4-C_5 bond.

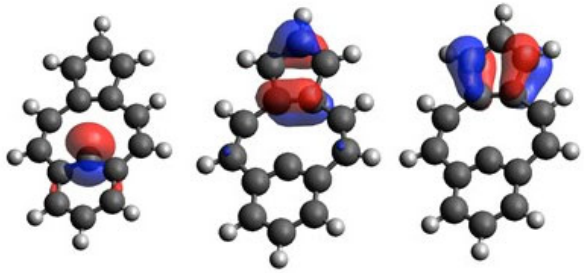

$^3B_1/^1B_1$	$(25a_1)^1$	$(5b_1)^1$	$(3a_2)^2$	[75.8/75.8]
$^3A_2/^1A_2$	$(25a_1)^1$	$(5b_1)^2$	$(3a_2)^1$	[75.8/75.8]
$^1A''/^3A''$	$(30a')^1$	$(29a')^2$	$(21a'')^1$	[61.8/75.7]
$^3A'$	$(30a')^1$	$(29a')^1$	$(21a'')^2$	[75.8]

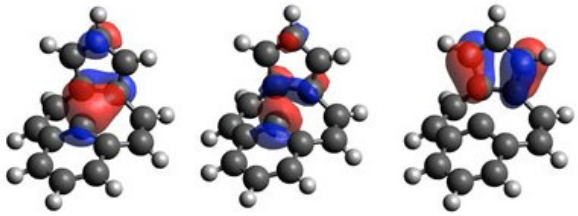

$^1A'$	$(29a')^2$	$(30a')^0$	$(21a'')^2$	[75.7]

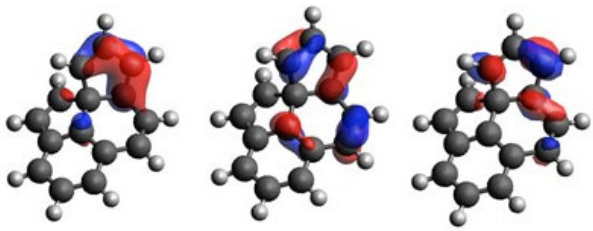

^1A	$(49a_1)^2$	$(50a_1)^2$	$(51a_1)^0$	[72.4]

Figure 5. The molecular orbitals of the dominant electron configurations where the values in brackets are the percent contributions calculated at the MR-CISD(4,3)/6-31G* level of theory.

Figure 5 shows the MOs of the SA4-CASSCF(4,3) active space and the dominant configuration for the singlet and triplet states of the different symmetry cases with the MR-CISD(4,3) method. The shorter C_4-C_5 bonds in the A_2 and A" states (Table 1) are due to the π-bonding character of the doubly occupied $5b_1$ (or the C_s counterpart 29a') orbital. The B_1 and A' states have longer C_4-C_5 bond lengths due to the singly occupied $5b_1$ or 29a' orbitals in the reference configuration. They have shorter C_2-C_4 bonds due to the π-bonding character of the doubly occupied $3a_2$ (or the C_s counterpart 21a") orbital. The optimized geometry of the non-planar

^{1}A' state has an L shape due to the interaction between the dangling bond orbital and the C_4-C_5 π orbital generating a bonding and an antibonding orbital combination, 29a' and 30a', respectively. Only the bonding orbital is occupied in the reference configuration resulting in a bonding interaction between C_{10}, C_4 and C_5, forming a three center and two electron (3c-2e) bond. A similar bonding interaction does not occur for other states leading to a bowl-shaped geometry to reduce repulsion between electrons of the dangling bond carbon and those of the C_4-C_5 bond. As discussed before, the ^{1}A' state can further distort into the ^{1}A state of C_1 symmetry to form a full covalent bond between C_{10} and C_4 or C_5.

3.3. Excited States of the Defect Structures

A comparison of vertical excitation energies for the planar pyrene-1C structures computed at MR-CISD+Q(6,6) level and using the optimized SA4-CASSCF(4,3) geometries of the 1^3B_1, 1^3A_2, $^1B_1$, and 1^1A_2 states is given in Figure 6. Numerical values can be found in Tables S7 – S10). Common to all spectra based on the different optimized geometries are the densely packed four lowest states (1^3B_1, 1^3A_2, 1^1B_1, and 1^1A_2), separated by a vertical excitation energy lower than 1 eV. All of these states have an open-shell configuration, where the first singlet state and the first triplet state differ only due to spin multiplicity, resulting in the triplet state being slightly more stable than the singlet for the same state symmetry. The lowest state differs according to the state of the geometry optimized.

Besides the difference between the lowest states of A_2 and B_1 for different geometries, higher excited states have similar excitation energies and oscillator strengths. For all four geometries, there is an energy gap of about 3 eV between the group of four lowest states and the remaining ones. The most intense excitations are always to the 4 $^1A_2$ state with an excitation energy of 7.6 eV to 7.8 eV. The second most intense excitation is to the 2^1A_2 state, though the intensity is much lower. An analysis of the excitation processes in terms of orbital excitations is given in Figures S2 and S3 for the 1^3B_1 and 1^3A_2 geometries, respectively. Most of the primary electron configurations describe single excitations. However, it should be noted that there are also doubly excited states occurring such as the 4 $^3A_2$ and 3 $^1A_2$ states in Figure S2.

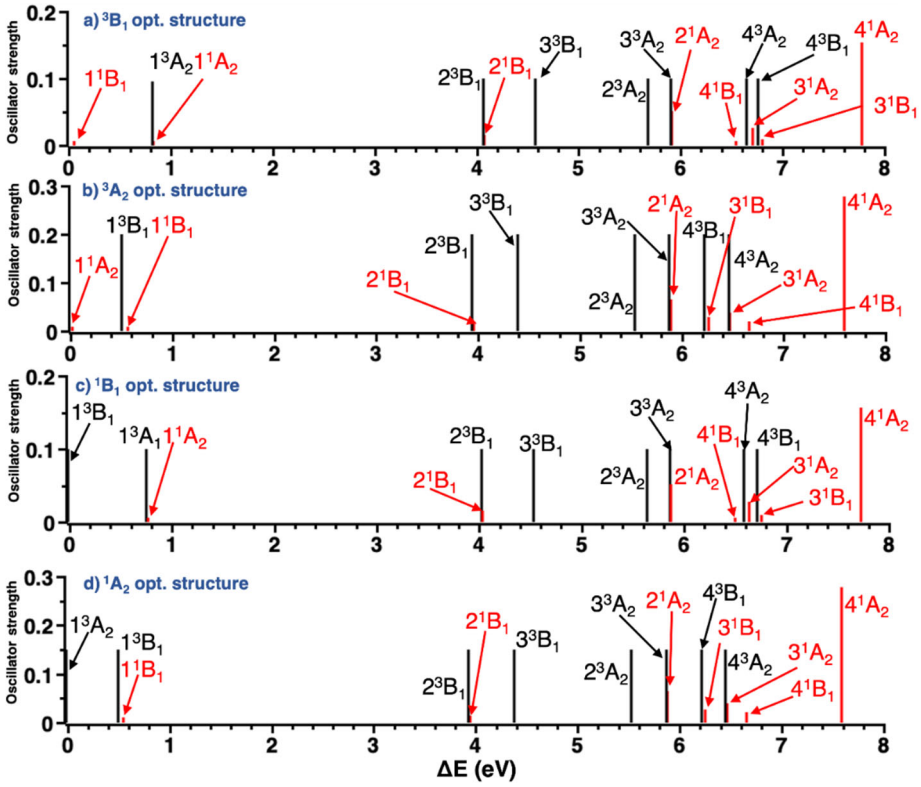

Figure 6. Vertical excitation energies ΔE (eV) for the respective optimized structure relative to the 1^3B_1 energy in spectrum a) computed at the MR-CISD+Q(6,6) level. Optimized geometries were obtained from SA4-CASSCF(4,3) calculations. Oscillator strengths refer to the singlet states (red vertical lines). For triplet states, black vertical lines only indicate the energetic position of the electronic state.

Vertical excitation energies were also computed for the oop-optimized geometries of the four lowest states $1^3A''$, $1^3A'$, $1^1A''$, and $1^1A'$ of C_s symmetry (Figure 7) (numerical data are collected in Tables S11-S14). For the geometries optimized for the $1^3A''$,$1^3A'$, and $1^1A''$ states (Figure 7a-c), the four lowest states are also densely packed within 1 eV but the singlet excitations are all of much lower intensity in comparison to the intensities found for the planar geometries (Figure 6). An orbital excitation analysis of the computed excited states is given in Figures S4 and S5. The most intense transitions for the $^1A''$ and $^3A''$optimized geometry (Figure 7a and c, respectively) involve an excitation to the $4^1A''$ state (oscillator strength of 0.045), due to orbital excitation from 29a' to 22a" (Figure S4) in the $1^1A''$ geometry, whereas for the $1^3A'$ geometry (Figure 7b) the most intense singlet transition is to $2^1A'$ (oscillator strength of 0.024), due to orbital

excitation from 26a' to 29a' (Figure S5). Doubly excited states are noted for the $1^3A'$ reference structure.

The $1^1A'$ optimized geometry results in a strongly stabilized $1^1A'$ state of closed-shell character (Table S14) with a doubly occupied bonding orbital (29a') with a (3c-2e) bond. The excitation spectrum is quite different in this case because of the closed-shell ground state structure. The first three excited states ($1^3A''$, $1^1A''$, and $1^3A'$) have open-shell configurations and are about 3eV higher in energy compared to $1^1A'$ (Figure 7d). This value is much larger than the excitation gap of < 1 eV found for all other structures. Oscillator strengths can be as high as 0.285 for transition to the 4 $^1A''$ state. The second most intense singlet transition is to $3^1A''$ ($f = 0.260$).

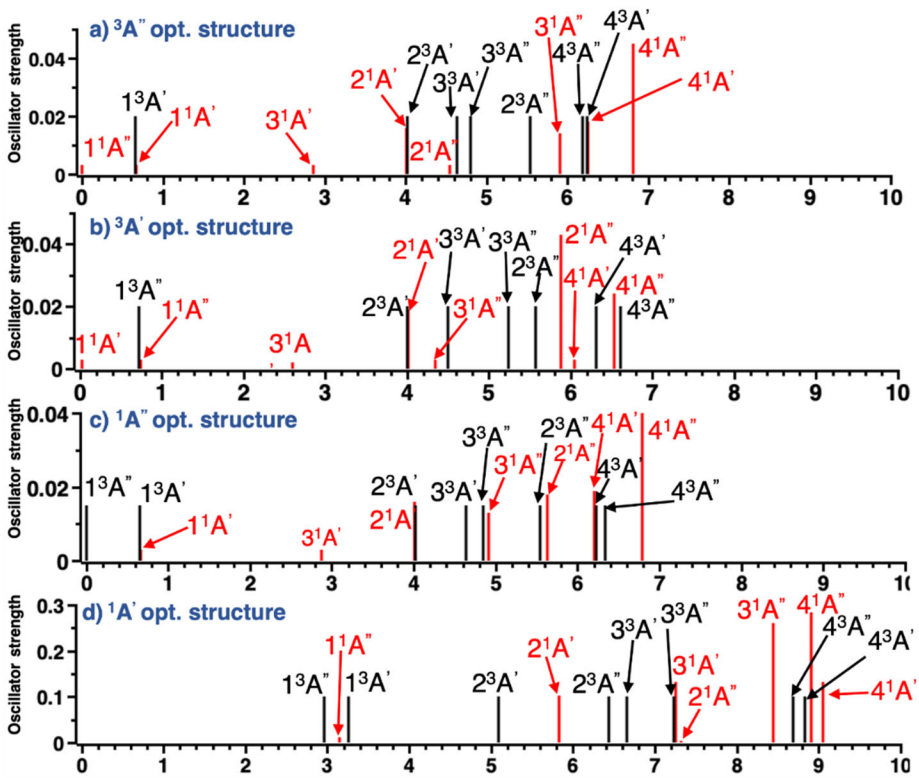

Figure 7. Vertical excitation energies ΔE (eV) for the respective optimized structure relative to the $1^3A''$ energy in spectrum a) computed at the MR-CISD+Q(6,6) level. Optimized geometries were obtained from SA4-CASSCF(4,3) calculations. Oscillator strengths refer to the singlet states (red vertical lines). For triplet states, black vertical lines only indicate the energetic position of the electronic state.

4. Conclusions

The ability of a single-vacancy defect in a graphene sheet to deform from planarity was investigated using a pyrene model. The C_4-C_5 bond distance, originating from a bond formation of two of the three dangling bonds formed initially in the SV defect, showed distinct and characteristic values distinguishing between the B_1 and A_2 state symmetries. For planar structures (C_{2V} point group), the $^3B_1$ state was found as the ground state with the $^1B_1$, $^3A_2$, and $^1A_2$ excited states being closely spaced within about 0.1-0.2 eV. These properties varied little with the size of CAS ranging from the complete π-space CASSCF(16,16) to the more compact SA4-CASSCF(4,3) calculations. Extended MR-CISD calculations did not change that picture either. The planar structures all represented saddle points leading to geometries displaced from planarity. Probably one of the most interesting structures is the L-shaped $^1A'$ state (C_S symmetry), which is stabilized by about 0.22-0.53 eV with CASSCF and 1.13 eV with MR-CISD+Q, respectively, compared to planar structures. This stabilization is derived from the formation of a 3c-2e bond. Further relaxation of this singlet state to the C_1 point group forms a bond between the dangling carbon and one of those of the cyclopentadiene ring strongly deforming the pyrene and stabilizing the ^1A structure by about 3.25 eV compared to the planar structure. Another, somewhat less stable triplet state structure of C_1 symmetry was found also. In addition to the stable structures of C_1 symmetry, two shallow C_S minima exist without any additional CC σ bond formation.

These results were confirmed with MR-CISD(4,3) calculations and further vertical excited states were calculated for each C_{2V} and C_S geometry using this method. For the planar structures, the lowest four states are energetically closely packed and followed by an energy gap of about 3 eV separating the higher excited states. For the non-planar C_S structures, the energetically close packing of the four lowest states is preserved from the planar geometries.

Previous calculations[13] on larger graphene SV defect models based on planar circum-pyrene and 7armchair (a),7zigzag (z) periacene showed that the basic electronic structure of the defect remained unchanged in comparison to the pyrene-SV model. In all cases, the ground state is a triplet state. For the largest system, the 7a,7z-periacene, the lowest lying states are closer in energy for the larger systems, since there are more π orbitals close in energy for interaction available. The bridging C_4-C_5 bond length increases by 15 – 20% between the optimized pyrene-

SV and 7a,7z-periacene structures due to the restrictions of the enlarged honeycomb environment. Thus, the model of embedded localized states is predicted to be applicable with smaller quantitative modifications for lager graphene sections as well.

The consequences of oop distortions in a single carbon vacancy in an extended graphene can be analyzed based on the results of the present pyrene model system. In a larger sheet, greater geometrical forces will exist restraining the defect toward planarity. While the moderately deformed oop structures for the ^{3}A', ^{3}A", ^{1}A" states will persist in the present form, the highly deformed L-shaped ^{1}A' structure will be more restricted toward a planarized structure. However, it is expected that the subsequent σ bond formation with the strong stabilization of ~2.7 eV will be feasible. An investigation of defect structures embedded in a larger graphene sheet environment would be necessary to answer this question conclusively.

Supporting Information

Tabulated natural orbitals occupations, excitation energies, C-C bond distances, and electron configurations of the electronic states and structures calculated with the various CASSCF and MR-CISD methods. Orbital excitation diagrams for the MR-CISD(6,6) method. Cartesian coordinates of all optimized structures.

Acknowledgments:

This research was funded by Brazilian agencies São Paulo Research Foundation (FAPESP), grant numbers 2018/13673-7 and 2022/16385-8 and Conselho Nacional de Desenvolvimento Científico e Tecnológico (CNPq), grant number 307168/2022-0. Support by the USA National Science Foundation under Grant No. 2107923 is gratefully acknowledged. We also thank for ample computer time at the computational facilities of the High-Performance Computer Center of Texas Tech University.

References:

(1) Novoselov, K. S.; Geim, A. K.; Morozov, S. V.; Jiang, D.; Zhang, Y.; Dubonos, S. V.; Grigorieva, I. V.; Firsov, A. A. Electric Field Effect in Atomically Thin Carbon Films. *Science* **2004**, *306*, 666-669.
(2) Geim, A. K.; Novoselov, K. S. The rise of graphene. *Nat. Mater.* **2007**, *6*, 183-191.
(3) Castro Neto, A. H.; Guinea, F.; Peres, N. M. R.; Novoselov, K. S.; Geim, A. K. The electronic properties of graphene. *Rev. Mod. Phys.* **2009**, *81*, 109-162.
(4) Cheng, R.; Bai, J.; Liao, L.; Zhou, H.; Chen, Y.; Liu, L.; Lin, Y.-C.; Jiang, S.; Huang, Y.; Duan, X. High-frequency self-aligned graphene transistors with transferred gate stacks. *Proc. Natl. Acad. Sci. U. S. A.* **2012**, *109*, 11588-11592.
(5) Wu, Y.; Jenkins, K. A.; Valdes-Garcia, A.; Farmer, D. B.; Zhu, Y.; Bol, A. A.; Dimitrakopoulos, C.; Zhu, W.; Xia, F.; Avouris, P.; et al. State-of-the-Art Graphene High-Frequency Electronics. *Nano Lett.* **2012**, *12*, 3062-3067.
(6) Bonaccorso, F.; Sun, Z.; Hasan, T.; Ferrari, A. C. Graphene photonics and optoelectronics. *Nat. Photonics* **2010**, *4*, 611-622.
(7) Lu, G.; Yu, K.; Wen, Z.; Chen, J. Semiconducting graphene: converting graphene from semimetal to semiconductor. *Nanoscale* **2013**, *5*, 1353-1368.
(8) Wu, J.; Pisula, W.; Müllen, K. Graphenes as Potential Material for Electronics. *Chem. Rev.* **2007**, *107*, 718-747.
(9) Kotakoski, J.; Krasheninnikov, A. V.; Kaiser, U.; Meyer, J. C. From Point Defects in Graphene to Two-Dimensional Amorphous Carbon. *Phys. Rev. Lett.* **2011**, *106*, 105505.
(10) Hashimoto, A.; Suenaga, K.; Gloter, A.; Urita, K.; Iijima, S. Direct evidence for atomic defects in graphene layers. *Nature* **2004**, *430*, 870-873.
(11) Meyer, J. C.; Kisielowski, C.; Erni, R.; Rossell, M. D.; Crommie, M. F.; Zettl, A. Direct Imaging of Lattice Atoms and Topological Defects in Graphene Membranes. *Nano Lett.* **2008**, *8*, 3582-3586.
(12) Machado, F. B. C.; Aquino, A. J. A.; Lischka, H. The Diverse Manifold of Electronic States Generated by a Single Carbon Defect in a Graphene Sheet: Multireference Calculations Using a Pyrene Defect Model. *ChemPhysChem* **2014**, *15*, 3334-3341.
(13) Pinheiro, M.; Cardoso, D. V. V.; Aquino, A. J. A.; Machado, F. B. C.; Lischka, H. The characterization of electronic defect states of single and double carbon vacancies in graphene sheets using molecular density functional theory. *Mol. Phys.* **2019**, *117*, 1519-1531.
(14) Zhang, Y.; Li, S.-Y.; Huang, H.; Li, W.-T.; Qiao, J.-B.; Wang, W.-X.; Yin, L.-J.; Bai, K.-K.; Duan, W.; He, L. Scanning Tunneling Microscopy of the π Magnetism of a Single Carbon Vacancy in Graphene. *Phys. Rev. Lett.* **2016**, *117*, 166801.
(15) Faccio, R.; Mombrú, A. W. Magnetism in multivacancy graphene systems. *J. Phys.: Condens. Matter* **2012**, *24*, 375304.
(16) Yazyev, O. V.; Helm, L. Defect-induced magnetism in graphene. *Phys. Rev. B* **2007**, *75*, 125408.
(17) Warner, J. H.; Rümmeli, M. H.; Ge, L.; Gemming, T.; Montanari, B.; Harrison, N. M.; Büchner, B.; Briggs, G. A. D. Structural transformations in graphene studied with high spatial and temporal resolution. *Nat. Nanotechnol.* **2009**, *4*, 500-504.

(18) Girit, Ç. Ö.; Meyer, J. C.; Erni, R.; Rossell, M. D.; Kisielowski, C.; Yang, L.; Park, C.-H.; Crommie, M. F.; Cohen, M. L.; Louie, S. G.; et al. Graphene at the Edge: Stability and Dynamics. *Science* **2009**, *323*, 1705-1708.
(19) Ugeda, M. M.; Brihuega, I.; Guinea, F.; Gómez-Rodríguez, J. M. Missing Atom as a Source of Carbon Magnetism. *Phys. Rev. Lett.* **2010**, *104*, 096804.
(20) Tapasztó, L.; Dobrik, G.; Nemes-Incze, P.; Vertesy, G.; Lambin, P.; Biró, L. P. Tuning the electronic structure of graphene by ion irradiation. *Phys. Rev. B* **2008**, *78*, 233407.
(21) Gnoffo, P. A. Planetary-Entry Gas Dynamics. *Annual Review of Fluid Mechanics* **1999**, *31*, 459-494.
(22) Vieira, L. d. S. A review on the use of glassy carbon in advanced technological applications. *Carbon* **2022**, *186*, 282-302.
(23) Prata, K. S.; Schwartzentruber, T. E.; Minton, T. K. Air–Carbon Ablation Model for Hypersonic Flight from Molecular-Beam Data. *AIAA Journal* **2022**, *60*, 627-640.
(24) Murray, V. J.; Recio, P.; Caracciolo, A.; Miossec, C.; Balucani, N.; Casavecchia, P.; Minton, T. K. Oxidation and nitridation of vitreous carbon at high temperatures. *Carbon* **2020**, *167*, 388-402.
(25) Murray, V. J.; Minton, T. K. Gas-surface interactions of atomic nitrogen with vitreous carbon. *Carbon* **2019**, *150*, 85-92.
(26) Murray, V. J.; Smoll, E. J., Jr.; Minton, T. K. Dynamics of Graphite Oxidation at High Temperature. *J. Phys. Chem. C* **2018**, *122*, 6602-6617.
(27) Wang, Y.; Nieman, R.; Minton, T. K.; Guo, H. Insights into adsorption, diffusion, and reactions of atomic nitrogen on a highly oriented pyrolytic graphite surface. *J. Chem. Phys.* **2021**, *154*, 074708.
(28) Jayee, B.; Nieman, R.; Minton, T. K.; Hase, W. L.; Guo, H. Direct Dynamics Simulations of Hyperthermal $O(^3P)$ Collisions with Pristine, Defected, Oxygenated, and Nitridated Graphene Surfaces. *J. Phys. Chem. C* **2021**, *125*, 9795-9808.
(29) Paci, J. T.; Paci, I. Theoretical Studies of the Reactions between Hyperthermal $O(^3P)$ and Graphite: Holes and the Second Layer. *J. Phys. Chem. C* **2019**, *123*, 29647-29655.
(30) Nieman, R.; Spezia, R.; Jayee, B.; Minton, T. K.; Hase, W. L.; Guo, H. Exploring reactivity and product formation in $N(^4S)$ collisions with pristine and defected graphene with direct dynamics simulations. *J. Chem. Phys.* **2020**, *153*, 184702.
(31) Nieman, R.; Aquino, A. J. A.; Lischka, H. Exploration of Graphene Defect Reactivity toward a Hydrogen Radical Utilizing a Preactivated Circumcoronene Model. *J. Phys. Chem. A* **2021**, *125*, 1152-1165.
(32) Szalay, P. G.; Müller, T.; Gidofalvi, G.; Lischka, H.; Shepard, R. Multiconfiguration Self-Consistent Field and Multireference Configuration Interaction Methods and Applications. *Chem. Rev.* **2012**, *112*, 108-181.
(33) Lischka, H.; Nachtigallová, D.; Aquino, A. J. A.; Szalay, P. G.; Plasser, F.; Machado, F. B. C.; Barbatti, M. Multireference Approaches for Excited States of Molecules. *Chem. Rev.* **2018**, *118*, 7293-7361.
(34) Machado, F. B. C.; Aquino, A. J. A.; Lischka, H. The electronic states of a double carbon vacancy defect in pyrene: a model study for graphene. *Phys. Chem. Chem. Phys.* **2015**, *17*, 12778-12785.
(35) Nieman, R.; Das, A.; Aquino, A. J. A.; Amorim, R. G.; Machado, F. B. C.; Lischka, H. Single and double carbon vacancies in pyrene as first models for graphene defects: A survey of the chemical reactivity toward hydrogen. *Chem. Phys.* **2017**, *482*, 346-354.

(36) Nieman, R.; Aquino, A. J. A.; Hardcastle, T. P.; Kotakoski, J.; Susi, T.; Lischka, H. Structure and electronic states of a graphene double vacancy with an embedded Si dopant. *J. Chem. Phys.* **2017**, *147*, 194702.
(37) Reimers, J. R.; Sajid, A.; Kobayashi, R.; Ford, M. J. Understanding and Calibrating Density-Functional-Theory Calculations Describing the Energy and Spectroscopy of Defect Sites in Hexagonal Boron Nitride. *J. Chem. Theory Comput.* **2018**, *14*, 1602-1613.
(38) Ruedenberg, K.; Cheung, L. M.; Elbert, S. T. MCSCF optimization through combined use of natural orbitals and the Brillouin–Levy–Berthier theorem. *Int. J. Quantum Chem.* **1979**, *16*, 1069-1101.
(39) Roos, B. O.; Taylor, P. R.; Siegbahn, P. E. M. A complete active space SCF method (CASSCF) using a density matrix formulated super-CI approach. *Chem. Phys.* **1980**, *48*, 157-173.
(40) Lischka, H.; Shepard, R.; Müller, T.; Szalay, P. G.; Pitzer, R. M.; Aquino, A. J. A.; Araújo do Nascimento, M. M.; Barbatti, M.; Belcher, L. T.; Blaudeau, J.-P.; et al. The generality of the GUGA MRCI approach in COLUMBUS for treating complex quantum chemistry. *J. Chem. Phys.* **2020**, *152*, 134110.
(41) Hehre, W. J.; Ditchfield, R.; Pople, J. A. Self—Consistent Molecular Orbital Methods. XII. Further Extensions of Gaussian—Type Basis Sets for Use in Molecular Orbital Studies of Organic Molecules. *J. Chem. Phys.* **2003**, *56*, 2257-2261.
(42) Hariharan, P. C.; Pople, J. A. The influence of polarization functions on molecular orbital hydrogenation energies. *Theor. Chim. Acta* **1973**, *28*, 213-222.
(43) Das, A.; Müller, T.; Plasser, F.; Lischka, H. Polyradical Character of Triangular Non-Kekulé Structures, Zethrenes, p-Quinodimethane-Linked Bisphenalenyl, and the Clar Goblet in Comparison: An Extended Multireference Study. *J. Phys. Chem. A* **2016**, *120*, 1625-1636.
(44) Langhoff, S. R.; Davidson, E. R. Configuration interaction calculations on the nitrogen molecule. *Int. J. Quantum Chem.* **1974**, *8*, 61-72.
(45) Lischka, H.; Müller, T.; Szalay, P. G.; Shavitt, I.; Pitzer, R. M.; Shepard, R. COLUMBUS—a program system for advanced multireference theory calculations. *WIREs Comp. Mol. Sci.* **2011**, *1*, 191-199.
(46) Werner, H.-J.; Knowles, P. J.; Knizia, G.; Manby, F. R.; Schütz, M. Molpro: a general-purpose quantum chemistry program package. *WIREs Comp. Mol. Sci.* **2012**, *2*, 242-253.

TOC Graphic